Materials Research Bulletin 196 (2026) 113899

Contents lists available at ScienceDirect

Materials Research Bulletin

journal homepage: www.elsevier.com/locate/matresbu

Research Papers

Influence of the graphene oxide precursor in laser-synthetized hybrid photocatalysts for the H_2 production by glycerol photoreforming

María Susana Gutiérrez [a], José Peral [b], Dominique Buyens [c], Enikö György [a,d], Ángel Pérez del Pino [a,*]

[a] Institute of Materials Science of Barcelona, Spanish National Research Council (ICMAB-CSIC), Campus UAB, Bellaterra 08193, Spain
[b] Department of Chemistry, Autonomous University of Barcelona, Bellaterra 08193, Spain
[c] Karlsruhe Institute of Technology, Institute of Microstructure Technology, Hermann-von-Helmholtz Platz 1, Eggenstein-Leopoldshafen 76344, Germany
[d] National Institute for Lasers, Plasma and Radiation Physics, PO Box MG 36, Bucharest 77125, Romania

ARTICLE INFO

Keywords:
Laser-assisted synthesis
H_2 production
Photocatalysis
Hybrid composites

ABSTRACT

The present study reports the versatile synthesis of photocatalysts composed of nitrogen-doped reduced graphene oxide (NrGO) flakes coated with TiO_2-FeO_x nanostructures using ultraviolet (UV) pulsed laser irradiation in a liquid environment. Different commercial graphene oxide (GO) sources were used, revealing a significant influence on the structural, compositional, and functional properties of the final photocatalysts. The H_2 production via water-splitting reaction using glycerol as sacrificial agent (photoreforming), ranged from 0.06 to 2.1 μmol H_2/g in 3.5 h depending on the GO precursor used. The best photocatalysts were those that showed a reduction in the TiO_2 material with a Ti(IV)/Ti(III) atomic ratio about 2.0–2.4, as well as a reduction and N-doping of GO, with 20–23 at % of C, and 4–6 at % of N. The light-scattering nature of the photocatalysts also had a significant effect on the H_2 production yield.

1. Introduction

Water splitting is a promising method for sustainable hydrogen generation, offering a clean energy source with water as its only byproduct [1,2] Among the various techniques, photocatalytic water splitting stands out for its simplicity and direct use of sunlight, making it a cost-effective and renewable alternative to electrocatalysis [3] Although its efficiency remains lower, ongoing research into advanced materials and hybrid systems is steadily improving its performance.

Photoreforming of sacrificial agents has further enhanced hydrogen production by converting waste into fuel [4,5] Photocatalysts used in these processes are typically semiconductors that harness solar energy to drive reactions. Common materials include metal oxides, sulphides, nitrides, and emerging 2D, composite, and heterojunction structures [6–15] Titanium dioxide (TiO_2) is widely studied due to its stability and non-toxicity, but its wide bandgap restricts absorption to UV light, which comprises only about 5 % of solar energy [16,17] To address this, researchers have explored doping TiO_2 with metals or non-metals and coupling it with cocatalysts to improve visible light absorption and reduce electron-hole recombination.

Graphene-based materials have emerged as highly effective co-catalysts. Their exceptional electrical conductivity facilitates rapid electron transport, minimizing recombination losses [15,18] Additionally, graphene's large surface area provides abundant active sites for hydrogen evolution. When combined with semiconductors like TiO_2, g-C_3N_4, or CdS, graphene acts as an electron acceptor, enhancing charge separation and structural stability, while reducing photocorrosion and improving long-term durability [19–22] Nitrogen-doped reduced graphene oxide (NrGO) offers further advantages. Nitrogen doping improves electronic properties and promotes Schottky junction formation, boosting charge transfer and hydrogen production efficiency [22–24] However, the structure of graphene oxide (GO) is inherently defective and varies with synthesis methods, affecting the functional properties of derived materials. This variability poses a challenge for practical applications.

Photocatalyst synthesis is a dynamic field, with techniques like sol-gel, hydrothermal, and chemical vapor deposition commonly used to produce materials with controlled morphology and crystallinity [25–27] Despite their effectiveness, these methods face limitations such as long processing times, precursor contamination, particle aggregation, and

* Corresponding author.
E-mail address: aperez@icmab.es (Á.P. del Pino).

https://doi.org/10.1016/j.materresbull.2025.113899
Received 17 June 2025; Received in revised form 5 November 2025; Accepted 18 November 2025
Available online 20 November 2025

scalability issues. As a result, alternative approaches are being explored. Laser-based synthesis offers several advantages: direct material formation from precursors, rapid production, and precise control over structure and doping. Techniques like matrix-assisted pulsed laser evaporation have been used to deposit thin-film hybrid photocatalysts for organic degradation [28–30] More notably, laser synthesis in liquid environments enables the direct production of metal, metal oxide, carbon, and hybrid photocatalysts, including NrGO-based systems for hydrogen generation [31–35] These methods involve high-energy photochemical and photothermal processes, such as laser-induced reactions, fragmentation, melting, ablation, and plasma formation.

In this study, we present a liquid-phase laser synthesis method for creating a hybrid photocatalyst composed of N-doped rGO flakes decorated with TiO_2–FeO_x nanostructures. A two-step process was designed: (i) simultaneous reduction and N-doping of GO sheets, and (ii) decoration with TiO_2–FeO_x nanostructures via laser irradiation of aqueous dispersions containing GO, imidazole, and metal-organic precursors (Ti-isopropoxide and Fe (III) nitrate). This versatile technique enables the formation of ternary systems combining 2D graphene-based materials with inorganic nanoparticles. A key focus of the study was the impact of the initial GO composition on the structural and functional properties of the resulting photocatalyst. Different commercial GO sources (Graphenea and Nanoinnova, in slurry and powder forms) were characterized and used in synthesis. Significant differences were observed in bandgap energies (2.1–3.2 eV) and hydrogen generation yields (0.06 to 2.1 μmol/g over 3.5 h), highlighting the importance of GO precursor selection for optimizing photocatalytic performance.

2. Experimental

GO was purchased from Graphenea (powder and slurries) and Nanoinnova (powder) and used as received. Imidazole, titanium (IV) isopropoxide, and iron nitrate ($Fe(NO_3)_3 \cdot 9H_2O$) were purchased from Sigma-Aldrich and used as received. Four different GO sources were used in this study to compare their physicochemical properties and explore the photocatalytic results depending on the precursor source. Two dried powder materials, GO Nanoinnova (GO-pn) and GO Graphenea (GO-pg), and two aqueous dispersions with a concentration of ca. 2.5 wt.%, GO-slurry (GO-sg) and GO-slurry with lower content of sulphur (GO-sws). Laser irradiation experiments of the precursor dispersions were performed using a Nd:YAG laser (Brilliant B, Quantel) emitting 4 ns laser pulses at a wavelength of 266 nm with a repetition rate of 10 Hz. The pulse laser energy was set to 70 mJ, the spot dimensions were ca. 64 mm^2, and an accumulation of 500 pulses per gram of dispersion was applied to the reaction mixtures under constant stirring (500 rpm) inside a 100 mL quartz beaker. A total volume of 50 mL of the initial dispersion was employed. All the experiments were performed in two steps (Fig. 1): first, GO and imidazole were dispersed in an aqueous solution (50 mg each); in the second step, Ti isopropoxide (850 mg) and iron nitrate (260 mg) were added to the mixture, and after a few minutes of sonication and stirring, the mixture was irradiated again under the same conditions. Subsequently, the final products were centrifuged to separate the photocatalyst from the unreacted precursors, and the resulting solid was washed twice with Milli-Q water two times in order to remove the physisorbed entities. Each cleaning step involved the addition of Milli-Q water and centrifugation for 30 min at 8000 rpm. Finally, the photocatalyst samples (PC-sg, PC-sws, PC-pg, PC-pn) were dried overnight at 100 °C.

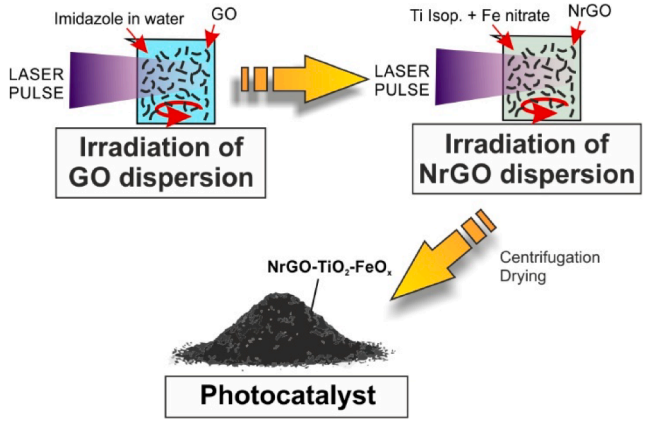

Fig. 1. Scheme of the synthetic method used for obtaining the photocatalysts.

The resultant solids were powdered using agate pestle and characterized by high resolution transmission electron microscopy (HRTEM) and high-angle annular dark-field (HAADF) mode using a FEI Tecnai G2 F20 microscope operating at 200 kV. The material composition was characterized by attenuated total reflectance Fourier-transform infrared spectroscopy (ATR-FTIR) using a Perkin-Elmer Spectrum One spectrometer. X-ray diffraction (XRD) measurements were performed using a Bruker D8 Advance A25 system (Cu K source) with a θ−2θ configuration in the 10–80° acquisition range. X-ray photoelectron spectroscopy (XPS) analysis was conducted using a K-alpha XPS spectrometer (Thermo Scientific TM) to examine the surface chemistry. The samples were excited with X-ray radiation from a monochromatic Al-Kα source (1468.6 eV). The spot size was 300 μm, and the pass energy for the narrow scan spectra was 25 eV. The spectrometer was equipped with a flood gun for charge compensation, any charge-induced energy shift being corrected by fixing the C1s line at 284.4 eV. ^{1}H NMR spectra were acquired at 500 MHz on a Bruker Elmar ultrashield 500 wide-bore system. The ^{1}H NMR spectra were calibrated using the DMSO-d_6 solvent peak at 2.50 ppm. Approximately 20 mg of reference samples dispersed in 0.5 mL of DMSO-d_6 (from Eurisotop) were sonicated for 5 min and analyzed. UV–Vis spectrophotometry characterization of the powder materials was done in the 200–800 nm operational range with a Jasco V-770 spectrophotometer using a DRA-2500 diffuse reflectance sphere accessory. The band gap energies were estimated using the Kubelka–Munk and Makula functions as published in previous works, and considering indirect allowed transitions [36,37] The same spectrophotometer was used for absorbance studies of 1 mg/mL aqueous dispersions of the powders after 10 min of sonication. The photoluminescence of the same dispersions was analyzed in the 300–550 nm range with a multimode Spark (TECAN) system, illuminating with a 274 nm excitation wavelength. Moreover, the size distribution of the particles was studied through dynamic light scattering (DLS) by using the Malvern Instruments Zetasizer Nano ZS for nanometric to sub-micrometric particle size and Mastersizer 2000 for micrometric – millimetric sizes distributions.

The hydrogen generation capability of the obtained products was assessed using water-glycerol solutions (photoreforming). The main element of this experimental set up was a double wall cylindrical Pyrex reactor of 125 mL volume, fitted with a gas inlet and outlet, connected to a thermostatic bath, and placed on a magnetic stirrer. Three lamps (15 W compact UVA lamps with an emission band centered at 380 nm) surrounding the reactor provided UVA-light radiation. In all experiments, 100 mg of catalyst was added to 50 mL of an aqueous solution of glycerol (0.25 M). The reactor was then closed, and the remaining air (~75 mL) was pumped out and replaced with pure N_2. Subsequently, the lamps were turned on and the solution irradiated. Hydrogen generation was assessed using gas chromatography with a Shimadzu GC-2014 chromatograph equipped with a packed column (Carboxen 1000 stationary phase) and a TCD detector. Injections were performed using a six-port injection valve with a fixed 2 mL volume loop. Besides, transient photocurrent measurements were conducted using a Keithley 2450-EC equipment and a home-made illuminating system composed of a 460 W high pressure UV lamp (OSRAM Supratec HTC400 241 R7s), a motorized chopper and a quartz cuvette. The samples were prepared in form of slurries containing 20 mg of the photocatalyst powder, mixed with 0.2 mL of aqueous solution of poly(vinyl alcohol) (PVA, Merck; 4

wt.%) and 0.2 mL of deionized water. After thorough sonication, the dispersions were dropped on ca. 1 cm^2 FTO glass substrates. After drying, copper stripes were glued to the FTO surface by means of silver paste. Chronoamperometry measurements were made in 0.5 M aqueous solution of Na_2SO_4 containing 5 wt.% of glycerol. The photocatalyst samples were used as working electrode and a Pt wire as counter electrode. The open circuit potential in dark conditions was applied during the measurements. Electrochemical impedance spectroscopy (EIS) characterization was also performed in dark conditions to the photocatalyst-PVA films in 0.5 M Na_2SO_4 aqueous electrolyte by means of a HIOKI IM3590 chemical impedance analyzer using a Ag/AgCl (3 M NaCl) reference electrode. Impedance was acquired in the 0.1 to 2×10^5 Hz frequency range, at the open circuit potential and applying 5 mV AC amplitude. Besides, Mott-Schottky characterization was carried out at 1 kHz frequency in the −0.5 to 1.5 V vs Ag/AgCl range, applying an amplitude of 10 mV. A waiting time of 10 min was taken at each potential before making the measurement for electrical stabilization of the film-electrolyte system.

Finally, photothermal simulations were carried out for unraveling the physicochemical mechanisms taking place upon the laser irradiation of the nanoentities inside the aqueous dispersion. The heat equation was solved in 2D finite element models of GO sheets and TiO_2 NPs in liquid water at room temperature by means of COMSOL Multiphysics 6.0 analyzer. The thermal and fluid dynamics physical modules were coupled. For the sake of easiness, the models used a Gaussian pulse evolution in time, as well as squared TiO_2 NPs and rectangular flakes of GO (half-length of 250 nm, use of horizontal symmetry) with 1–10 nm thickness (about 1–15 layers). The optical and thermophysical properties of GO, TiO_2 and H_2O were extracted from Refs [38–40]

3. Results and discussion

3.1. Compositional study of GO precursors

The chemical structure and composition, as well as functional properties of the GO material significantly differs between commercial manufacturers. In order to elucidate the chemical composition of the different raw GO precursors used in this study, they were thoroughly characterized by ATR-FTIR and XPS techniques. The ATR-FTIR spectra of the raw GO precursors are shown in Fig. S1a of Supplementary Material (SM). The wide peak at 3220 cm^{-1} is assigned to the O—H stretching, and the peaks at 1730 and 1620 cm^{-1} to the $C = O$ and $C = C$ stretching vibrations, respectively. A C—O stretching band appears at 1045 cm^{-1}, indicating a low amount of ether groups (C—O-C) [41] in the GO structure, with the exception of the GO-sws precursor. Besides, the GO-sws precursor presents two C—H bands at about 905 and 2905 cm^{-1}, which are not observed in the spectra of other GO precursors.

XPS analyses provide insights into the chemical composition of GO precursors. The comprehensive XPS surveys, depicted in Fig. S2, predominantly reveal the presence of carbon and oxygen, with minor quantities of nitrogen and sulphur. Table 1 presents the atomic percentages of these elements, indicating that carbon is the most abundant element (60.6 – 69.0 at.%), followed by oxygen (29.0 – 37.0 at.%). Among the samples, GO-sg exhibits the lowest carbon-to-oxygen (C/O) ratio (1.6), whereas GO-sws and GO-pg display the highest ratio (2.3). Typically, GO is expected to have a C/O ratio of 0.5–0.8, suggesting a partially reduced structure of the GO precursors [42] The nitrogen content is minimal, approximately 0.9 – 1.5 at.%, and sulphur is also present in low amounts, ranging from 0.5 – 1.0 at.%. Fig. S3 illustrates the high-resolution C1s spectra of the GO precursors, accompanied by tables detailing the deconvoluted peaks and their characteristics (position, full width at half maximum [FWHM], at.%). The components identified include $C = C$ (sp^2) at 283.8 – 284.2 eV, C—C (sp^3) at 284.8 – 285.2 eV, C—OH (alcohols or phenols) at 285.5 – 286.5 eV, C—O-C (ethers, esters, pyrans, anhydrides, or epoxy) at 286.7 – 287.0 eV, $C = O$ (carboxylic acids, ethers, ketones, anhydrides, or aldehydes) at 287.8 – 288.7 eV, and O—$C = O$ (carboxylic acids, esters, or anhydrides) at 288.8 – 290.1 eV, indicating slight variations among the GO materials [43] These findings are consistent with the chemical groups identified by Fourier-transform infrared spectroscopy (FTIR) (Fig. S1a). In all instances, the most prominent components are C—O-C (epoxy; approximately 30 at.%) and sp^3 C—C (approximately 20 at.%), with a relatively low presence of sp^2 $C = C$. This suggests a limited number of graphene domains and a structure characterized by numerous C—C and C—O bonds. The variations in the precursor spectra are associated with the quantities of C—O, $C = O$, and O—$C = O$ groups. The analysis of the deconvoluted O1s spectra corroborates the presence of $C = O$ / SO_x (531.0 – 531.4 eV), C—OH (532.8 – 533.3 eV), C—O-C (532.1 – 532.6 eV), and O—$C = O$ (533 - 534.3 eV) bonds (Fig. S4) [44,45] Notably, GO-sg contains a higher proportion of C—OH groups compared to its counterparts and a reduced amount of C—O-C groups, which may influence its reactivity and potentially account for the suboptimal performance of the derived photocatalyst (vide infra). In the context of N1s analysis, the spectra of all the raw graphene oxide (GO) precursors exhibit a primary peak corresponding to graphitic nitrogen (401.0 – 401.5 eV). Additionally, GO-sws reveals a minor component at 399.2 eV, attributed to pyridinic nitrogen or amine groups (Fig. S5) [46,47] The S2p spectra of all the raw GO precursors are characterized by a singular peak at approximately 168.3 eV, which is associated with oxidized sulphur (-SO_x) (Fig. S6). In summary, GO-sg demonstrates the highest oxygen-to-carbon ratio, the greatest abundance of C—OH groups, and the highest sulphur concentration within its structure. The GO-pn, GO-pg, and GO-sws precursors exhibit similar relative quantities of carbon-oxygen groups, with C—O-C groups being the most prevalent. Among these three compounds, GO-pn contains the largest amount of C—OH. Conversely, GO-sws displays the highest nitrogen content (as graphitic and pyridinic moieties) and the lowest sulphur content. Achieving a balance among these functional groups is crucial for optimal performance.

Table 1
XPS atomic percentage of C, O, N and S in the graphene oxide precursors, as well as reduction degree (C/O ratio). In comments: L = lowest, H = highest.

Precursor	C (at. %)	O (at. %)	N (at. %)	S (at. %)	C/O	Comments
GO-sg	60.6	37.0	1.5	1.0	1.6	(L) C/O; (H) C—OH and S
GO-sws	69.0	29.0	1.5	0.5	2.3	(H) N; (L) S; C—H bands (FTIR)
GO-pg	68.2	30.0	0.9	0.9	2.3	–
GO-pn	66.6	31.8	1.0	0.6	2.1	(2nd H) C-OH

3.2. Structural-compositional study of photocatalysts

For an overall understanding of the physicochemical mechanisms occurring during the synthesis process, the laser irradiation of the GO precursors in aqueous imidazole dispersions was simulated as a graphitic-like platelet inside liquid water irradiated with a single laser pulse. Given that the photon energy (4.7 eV) is higher than the dissociation energy of most of the molecular bonds contained in the GO material, [48–50] the photoexcited electrons are expected to generate photochemical processes [51] However, since the used laser fluence (0.11 J/cm^2) is below the ablation threshold, a substantial internal conversion of the absorbed photon energy to molecular vibrational modes can be considered, triggering a rapid heating and subsequent photothermal chemical reaction of the material [52] Note that: (i) the dissociation energy of $C = C$ sp^2 bonds (8.3 eV) [53] is much higher than the photon energy, pointing to a selective alteration of the GO domains with larger concentration of structural defects and carbon-oxygen bonds (lower dissociation energies); and (ii) water solvent is transparent to the UV radiation, but the imidazole molecules dissolved in the water could be also partially decomposed into reactive species. In order to consider

the effect of the GO dimensions on the thermal evolution, the thickness of the simulated platelets was set in the 1 – 10 nm range. Fig. 2a shows the calculated temperature at the surface of the irradiated GO sheets, which reveal a highly uniform temperature throughout their entire volume due to the high thermal conductivity of graphitic materials and the extremely thin nature of the sheets (Fig. 2b). As observed, the thinnest GO sheets (1 nm) barely heat up to a maximum temperature of ca. 40 °C and cool down rapidly upon the fade of the pulse intensity. However, thicker platelets experience a significant temperature leap at ca. 100–120 °C, followed by a subsequent increase to ca. 306 and 1345 °C, respectively, at 5 and 10 nm thickness. This sudden leap in the GO temperature is related to the phase transition of the surrounding liquid water to vapor (100 °C at atmospheric pressure). This covering vapor shell is characterized by a low mass density and thermal conductivity, acting as a barrier to the diffusion of the generated thermal energy to the environment (solvent), thus leading to a rapid increase of the GO temperature. Consequently, the rapid heating of the GO platelets is expected to induce their chemical modification, as already observed in similar experiments carried out within different liquid environments [34,54] As confirmed with FTIR analyses (Fig. S1b), the laser irradiation process leads to the reduction of C—O, $C = O$ signals of all the GO precursors, besides the appearing of N—H stretching signals at ca. 3200 cm^{-1} and 1550 cm^{-1}, as well as C—N stretching bands at about 1065 cm^{-1}. Noteworthy, laser irradiated GO-sg and especially GO-pg show less signal from the chemical groups than the other materials, indicating different chemical routes due to the raw GO physicochemical nature. Therefore, the first laser process allows a simultaneous photoreduction and N-doping of the GO sheets (referred to as NrGO) through the intense heating and chemical reaction with the partially decomposed imidazole molecules (which depends on the initial chemical composition and thickness of the GO precursor sheets). As a consequence, functional properties as the optical band gap of the NrGO materials become different, as observed in comparative raw GO - NrGO Tauc Plots (Fig. S7).

In the second laser irradiation step, Ti isopropoxide (main component) and Fe nitrate are added to the NrGO dispersion. The direct UV photoinduced decomposition of Ti isopropoxide into TiO_2 has been already evidenced [55] Besides, Ershov et al. demonstrated that the 266 nm laser radiation can lead to the direct photodissociation of Ti isopropoxide into Ti and TiO species, [56] which would be oxidized into TiO_2 within the reactive aqueous medium. Moreover, it is well known that the Ti isopropoxide spontaneously reacts with water, leading to the formation of TiO_2 nanocrystals. Consequently, it can be assumed that the dispersion submitted to laser irradiation contained TiO_2 nanoparticles (NPs) and dissolved Fe nitrate, in addition to the NrGO sheets. The thermal evolution of TiO_2 NPs upon the action of the UV laser pulses was also simulated (Fig. 2a, c). Similar to the GO case, a thermally insulating cavity of water vapor is created around the NPs with sizes larger than 3 nm, leading to an abrupt increase of the NP temperature beyond the TiO_2 melting (1872 °C) and vaporization (2972 °C) temperatures. The onset of such phase transitions decreases as the NP size increases (< 3 ns after the start of the laser pulse). In these extreme conditions, an energetic high-pressure plasma cavity comprised of atomic and ionic species is created, leading to a rich chemical interaction with the surrounding medium, which is vaporized producing a cavitation bubble [31] The fast laser-driven evaporation of the TiO_2 NPs and surrounding liquid is followed by the cavitation bubble collapse, leading to the rapid solidification of nanocrystallites and the formation of shockwaves that can even damage the quartz beaker containing the dispersion if a high concentration of precursors is used [57,58]

The TEM studies reveal the laser-induced crystallization of two different types of nanostructures, NPs and sphere-like, on the surface of the NrGO sheets (Fig. 3a). The NPs densely cover the NrGO surface and reveal sizes in the 1–10 nm range, approximately. The spherical nanostructures are less in number but bigger, about 20–150 nm in diameter, and they can appear as “filled” or “hollow” (shell-like). Hemispherical “filled” particles are also observed on the NrGO surface. The NPs covering the NrGO sheets would be created upon the multipulse laser

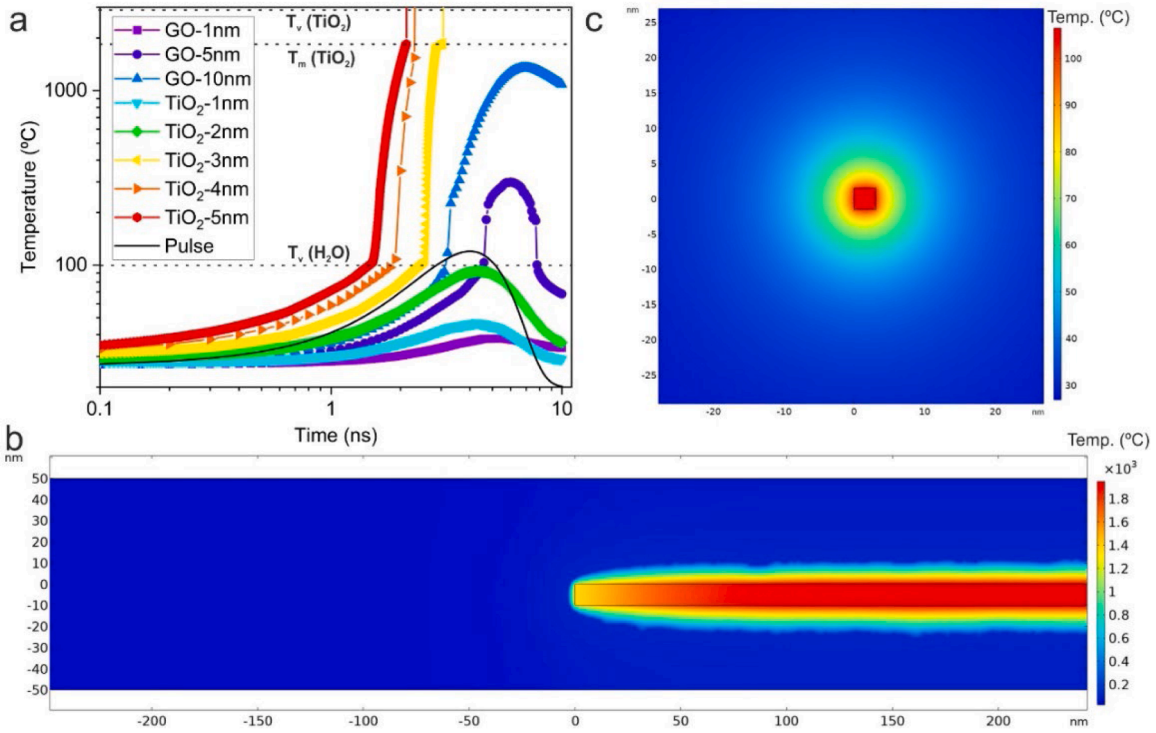

Fig. 2. (a) Simulated temperature as a function of time upon laser irradiation in GO sheets and TiO_2 NPs immerse in water as a function of their size. The time evolution of the laser intensity is also plotted. (b) Temperature map (@ 7 ns) of part of a GO sheet with 10 nm thickness. (c) Temperature map of a TiO_2 NP (3 nm in size) @ 2.5 ns.

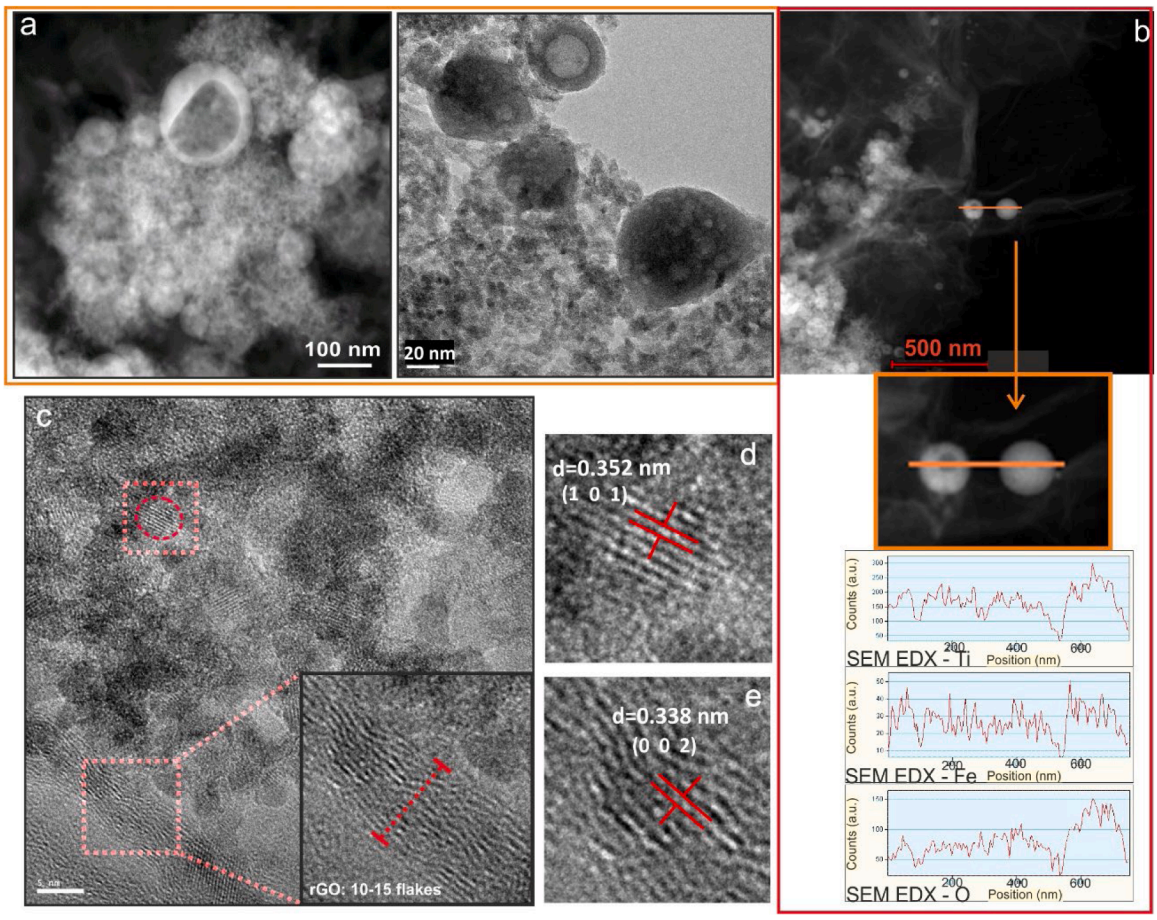

Fig. 3. (a) Typical HAADF and bright field TEM images of the PC-sg sample revealing the shell-like structures. (b) HAADF image revealing "bulk" and shell-like NPs, including the EDX element profiles of Ti, Fe and O along the indicated line-scan. (c) HRTEM image, with an inset of a zoomed area indicating 10–15 NrGO stacked layers. Magnified areas of (d) TiO_2 NP and (e) NrGO stacked layers, indicated in (c).

heating of the TiO_2 NPs present in the target dispersion. The smallest TiO_2 NPs adsorbed on the NrGO surface can reach the melting temperature, leading to the crystallization of larger particles due to diffusion and coalescence of the molten material. Indeed, the observed hemispherical particles could be an indication of such coalescence mechanisms. However, the transient bubbles created upon the vaporization of bigger TiO_2 NPs could trigger the formation of the observed hollow spheres, though other mechanisms as Kirkendall voiding effect were also proposed [59] In this case, the intense plasma explosion that occurs upon the laser-induced vaporization of the NPs would provoke the growth of micrometric cavitation bubbles with μs lifetime [60] The larger NPs generate bigger bubbles with faster expansion rate, a process that can be considered adiabatic. In this phase, the accumulation of supersaturated Fe solute at the vapor-liquid interface can occur due to the solvent evaporation [57] During the bubble collapse, the thermal energy exchange of the vapor with the surrounding liquid increases, leading to a rapid cool down and subsequent nucleation of nanocrystalline Ti, Fe oxides in form of filled or hollow spheres. It is also worth noting that the primary cavitation bubbles can be fragmented into secondary bubbles, creating smaller particles. Fig. 3b presents an EDX line-scan along similar spheres in size, being one of them clearly hollow (on the left). As observed, Ti, Fe and O signals overlap in the whole range, indicating that Ti and Fe oxides are not spatially separated. As expected, the "filled" particle exhibits more signal than the "hollow" one, due to the presence of a greater quantity of material.

The HRTEM analyses reveal the formation of highly crystalline nanostructures on the NrGO surface, which acts as a 2D support (Fig. 3c). All the studied crystalline domains, with sizes in the 1–10 nm range, belong to TiO_2 anatase phase (JCPDS 04–014–5762) being (101) the most common crystallographic plane identified (Fig. 3d). The small size and highly crystalline nature of the nanocrystals point toward highly energetic and fast nucleation-growth processes compatible with the described laser-induced mechanisms. Noteworthy, no Fe oxides were identified in any sample. Additionally, a detailed inspection at the edge of the NrGO sheets discloses their highly defective turbostratic nature with about 10–15 stacked layers, with an average interplanar distance of 0.34 nm ((002) planes; Fig. 3c-inset, e).

Additional XRD analyses provide valuable insights to understand the crystalline structure and composition of the synthetized photocatalysts. Fig. 4a shows the diffractograms of all the studied samples revealing a main contribution of polycrystalline anatase TiO_2, with a very intense Bragg peak at 25.34°, corresponding to (101) crystallographic planes. The cubic (101) crystallite size (Fig. 4b), calculated through the Scherrer equation, reveals a similar value about 4.0 – 4.4 nm in all the photocatalysts, except in PC-sg, which exhibits larger size (5.3 nm). This would indicate that most of the NPs observed by TEM, about 1–10 nm in size, are mainly single crystalline. Interestingly, at 30.81° appears a small signal assigned to (121) crystallographic planes of brookite TiO_2. The ratio of the deconvoluted (101) anatase / (121) brookite peaks area, shown in Fig. 4b, vary in the 0.04–0.23 range corresponding to PC-sg and PC-pg photocatalysts, respectively. Brookite is a rare metastable phase of TiO_2 that has attracted the research attention due to its photocatalytic activity. On the other hand, even though iron element was detected all over the samples by TEM-EDX, the presence of iron oxide phases was not detected through XRD, confirming their tiny concentration. The Bernal-stacked graphite pattern (JCPDS 00–056–0159) was

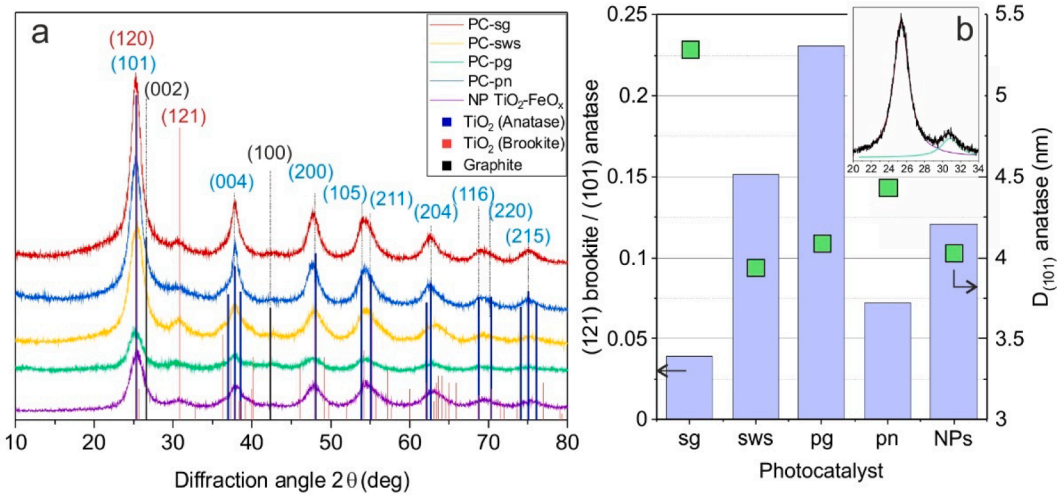

Fig. 4. (a) XRD plots of the obtained NrGO-TiO_2-FeO_x photocatalysts and TiO_2-FeO_x NPs. The reference patterns of TiO_2 (anatase; JCPDS 04–014–5762), TiO_2 (brookite, JCPDS 00–015–0875) and graphite (JCPDS 00–056–0159) are also included. (b) (101) anatase crystal size and ratio of the (121) brookite / (101) anatase peak areas. Inset: typical deconvolution of (101) anatase and (121) brookite peaks (PC-sws sample).

used as crystallographic reference for the NrGO material. The intensity of the NrGO peaks is extremely low, probably due to its low crystallinity compared to the metal oxides, being overlapped with the TiO_2 signal. Besides, no (001) GO peak at about 10° was recorded, pointing to a high reduction process of the GO material. The diffraction pattern of TiO_2-FeO_x NPs obtained by means of the second irradiation step (without the presence of NrGO), used as a reference, discloses very similar signal and crystallite size to that of the photocatalysts, indicating no significant influence of the NrGO sheets on the NPs formation, except the relative amount of anatase / brookite, besides the relative intensity of some anatase peaks, probably due to the contribution of overlapped NrGO peaks.

The compositional analysis of the photocatalysts was complemented with FTIR and XPS techniques. Figure S1c presents the FTIR spectra of the samples, which exhibit a prominent stretching band at 450 cm^{-1}, indicative of metal-O bonds, across all samples. The results also reveal a significantly weaker signal for the chemical bonds of the NrGO material, likely due to the presence of the TiO_2-based coating. Given that TiO_2 NPs strongly absorb UV laser radiation during synthesis, the structure of the NrGO sheets is expected to remain largely intact (shadow effect), preserving their functional properties. The XPS characterization provides a more detailed understanding of the synthesized photocatalysts' composition. As anticipated, the XPS wide scan analysis confirms the presence of C, O, N, Ti, and Fe (Fig. 5a). Notably, the sulphur initially

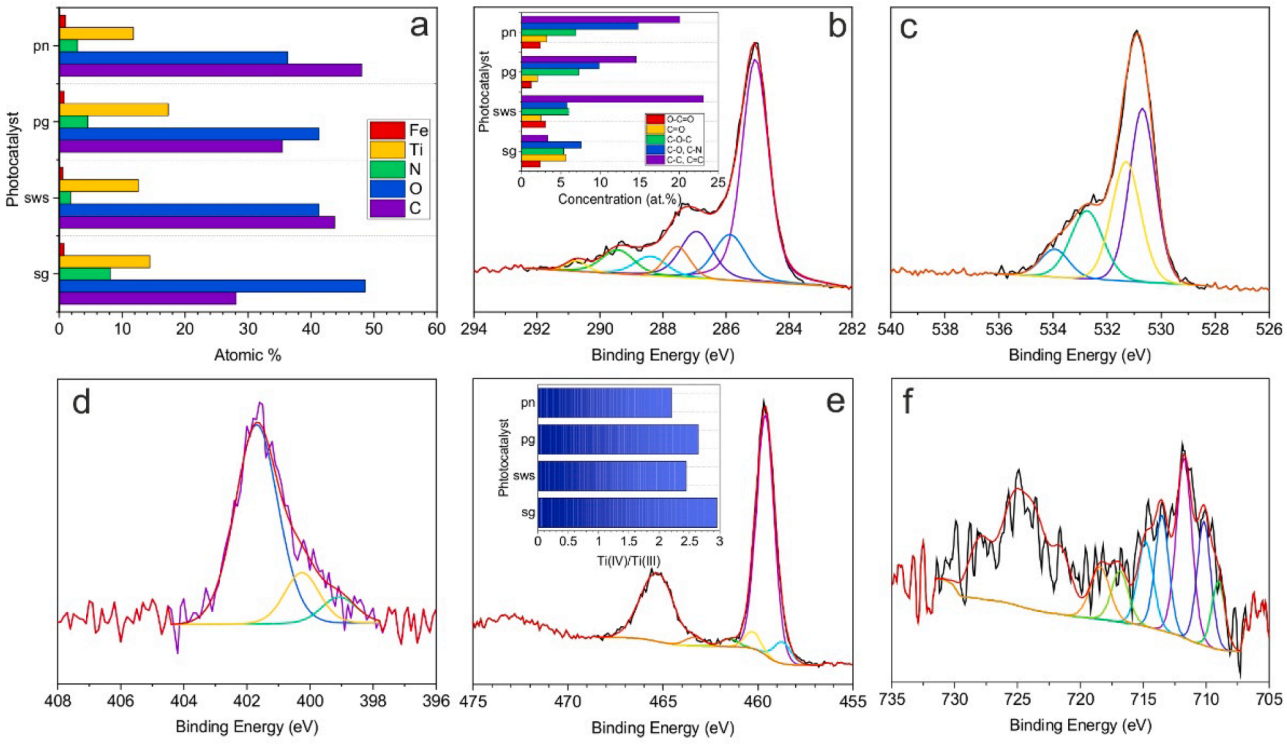

Fig. 5. (a) Elemental concentration recorded from XPS surveys. (b) C1s, (c) O1s, (d) N1s, (e) Ti2p, and (f) Fe2p XPS spectra of the PC-sws photocatalyst. Inset in (b): Atomic percentage of the C1s components in all the photocatalysts. Inset in (e): Ti(IV)/Ti(III) areal ratio of all the photocatalysts.

present in the GO precursors is absent in the NrGO structure, suggesting the active role of S-groups in chemical reactivity. Carbon is the most abundant element in PC-sws (ca. 44 at.%) and PC-pn (ca. 48 at.%) precursors, while oxygen is most prevalent in PC-sg (ca. 49 at.%) and PC-pg/PC-sws (ca. 41 at.%). The nitrogen content ranges from 1.8 at.% in PC-sws to 8.1 at.% in PC-sg. The titanium content varies between 11.8 at.% in PC-pn and 17.3 at.% in PC-pg, while iron is present in the smallest amounts, ranging from 0.6 at.% (PC-sws) to 1.0 at.% (PC-pn). The concentration of these elements associated with the NrGO component of the photocatalysts, as well as the related C/O and N/C ratios, can be calculated by subtracting the contribution of the O-Ti/Fe bonds present in the deconvoluted high-resolution O1s spectra, which will be described below. As depicted in Figure S8, the most reduced NrGO is the pn type ($C/O = 3.2$), followed by pg (2.3), sws (1.9), and sg (0.8). Interestingly, only the NrGO-pn exhibits a higher degree of reduction than the initial GO counterpart (Table 1), whereas NrGO-pg shows no difference, and the remaining NrGOs display a lower degree of reduction. This finding regarding reduction degrees differs from that derived from the C1s spectra (vide infra) and may be attributed to the hydroxylation of the TiO_2 NPs, whose contribution to O1s may be obscured by the C—O signal [61] Importantly, hydroxylated anatase demonstrates enhanced photocatalytic behaviour. Furthermore, the N-doping of the rGO structure is evident, with nitrogen content ranging from 1.8 to 8.1 at.%, significantly higher than the 0.5 to 1.5 at.% present in the initial GO precursors. The NrGO material with the highest nitrogen content is the sg type ($N/C = 0.30$), followed by pg (0.13), pn (0.06), and sws (0.04).

The high-resolution C1s photoemission spectra exhibit asymmetric tails at elevated binding energies (eV) (Fig. 5b, S9), indicative of diverse carbon bonding environments, the presence of oxygen and nitrogen-containing functional groups, and varying degrees of reduction [62] The spectral shape clearly suggests a reduction process when compared to the initial GO precursors (Fig. S3). In the deconvoluted C1s spectra, the C—C/$C = C$ bonds are considered to overlap at the same peak across all samples (284.0 – 285.0 eV), with PC-sws exhibiting the highest content (23.2 at.%; Fig. 5b inset) and a C—C to total C—O/N bond ratio of 1.34, which is notably higher than that of the other samples (see inset of Fig. 5b). PC-pg/PC-pn reveal a higher concentration of C—O bonds, indicating an incomplete reduction of GO to reduced graphene oxide (rGO) [63,64]. At 285.0 – 286.2 eV, C—O/C—N signals overlap, with PC-pn being the photocatalyst with the largest proportion of these functional groups. PC-sg displays an atypical C1s spectrum shape, where the peaks of C—O/C—N (285.3 eV, 6.55 at.%), C—O-C (286.2 eV, 4.80 at.%), and $C = O$ (287.1 eV, 5.96 at.%) are of similar proportions, and the C—C/$C = C$ (284.3 eV, 3.05 at.%) content is minimal. This observation suggests a significant transformation of the rGO material during the irradiation process [62,65,66] Notably, this material has the highest nitrogen content (Fig. S8) and the lowest atomic percentage of carbon bonds. It is likely that the high reactivity of the C—OH groups in GO-sg, which are predominant (Fig. S4), with imidazole molecules leads to a substantial decomposition of the rGO structure. Additionally, a minor peak attributed to C-Ti is observed in PC-pg and PC-sg at 282.8 – 283.1 eV, with 0.8 and 2.1 at.%, respectively, indicating the formation of a small quantity of titanium carbide nanoparticles facilitated by the extremely high temperatures during laser irradiation [67] The deconvoluted O1s spectra (Fig. 5c, S10) reveal a peak at 529.6 – 530.7 eV associated with O-Ti/Fe bonds of the TiO_2-FeO_x nanoparticles crystallized on the NrGO surface [37,68,69] The O-Ti/Fe peak is the most prevalent oxygen bond type in the photocatalysts, with PC-sg exhibiting the highest amount (27.6 at.%), and PC-sws the lowest O-Ti/Fe concentration (18.6 at.%). Other identified oxygen species include $C = O$ (530.1 – 531.3 eV), C—O (531.2 – 532.6 eV), and a small proportion of C—O-C (532.3 – 533.8 eV) [63,64,66]

The deconvoluted N1s spectra (Fig. 5d, S11) reveal various nitrogen species formed through laser-induced reactions with imidazole. All photocatalysts exhibit N-pyridinic (398.1–399.0 eV), N-pyrrolic (399.3–400.1 eV), and N-graphitic (400.6–401.9 eV) species [70,71] Notably, PC-sws shows a dominant N-graphitic signal, while the others display a more balanced presence of N-pyrrolic and N-graphitic species. Minor amounts of free –NH_x (401.7–402.0 eV) are also detected in PC-sg and PC-pn. Ti2p spectra (Fig. 5e, S12) confirm the presence of Ti(IV) from TiO_2 nanoparticles (458.6 eV [$2p_{3/2}$]) in all samples, along with a smaller contribution from Ti(III) (458.0 eV), indicating partial TiO_2 reduction. No Ti_2O_3 was observed via TEM or XRD. Reduced TiO_2 is known to enhance photocatalytic hydrogen evolution [72,73] The Ti (IV)/Ti(III) atomic ratio ranges from about 2 (33 % Ti(III)) in PC-pn to ca. 3 (25 % Ti(III)) in PC-sg. A small Ti-O_x signal in PC-sws suggests the presence of oxygen vacancies [68,74] Fe2p spectra (Fig. 5f, S13) show a multiplet structure, with Fe(III) as the dominant species and Fe(II) also present. Fe(II) peaks appear at 710.1 and 713.5 eV, while Fe(III) peaks are at 711.8 and 714.8 eV [75,76] Despite the noisy signal, the weak features located at 716.9 eV and 718.4 eV, could be respectively attributed to Fe(II) shake-up / Fe(III) surface satellite peak in Fe_3O_4 as well as Fe(III) shake-up satellite peak in Fe_2O_3 [76,77.] The Fe(II)/Fe (III) ratio (0.56–0.73) is consistent with Fe_3O_4, suggesting that FeO_x is primarily composed of magnetite [78] It is worth noting that TiO_2--magnetite photocatalysts are highly efficient systems for the removal of organic pollutants in wastewater [79,80] A distinct pre-peak at 708.9 eV, typical of small Fe-oxide nanoparticles on surfaces, supports the hypothesis of Fe supersaturation and crystallization at the vapor–liquid interface during laser-induced cavitation. In summary, XPS analysis confirms the simultaneous reduction and N-doping of GO, with varying nitrogen functionalities across samples. The high graphitic N content in PC-sws is particularly beneficial for enhancing charge transfer and suppressing recombination. Additionally, the photocatalysts feature partially reduced, hydroxylated TiO_2 and surface-decorated FeO_x nanoparticles, forming semiconductor nanojunctions that could support efficient charge carrier separation. For a deeper understanding of the chemical structure of the obtained materials, additional ^{1}H- NMR analyses were carried out to pn and pg materials, which show a minor presence of aliphatic groups as well as physi-, chemi-sorbed imidazole molecules (Fig. S14).

3.3. Functional properties of the photocatalysts

In regards to the functional properties investigation, all the powdered photocatalysts were studied by diffuse reflectance in order to calculate their band gap energy. Although the band gap energy is not a conclusive measure to predict the performance of a photocatalyst, it is capital to decrease the band gap of the material for increasing its optical absorption at the visible range, promoting an enhanced electron-hole pairs generation. The obtained Tauc plots of the photocatalysts are presented in Fig. 6a (indirect allowed transitions) [81] At a first glimpse, significant absorbance contributions are present at energies below the main band gap value, so the direct application of the Kubelka–Munk method could result in an inaccurate estimation. Makula et al. proposed an alternative method for these cases [36] Then, for the sake of correctness and comparison, the photocatalysts band gap energies were assessed following both Makula and Kubelka–Munk methods, respectively referred to as GAP 1 and GAP 2 (Table 2). The band gap of TiO_2-FeO_x NPs (without NrGO) is 2.3–2.7 eV (459–539 nm wavelength), which is lower than that of bare TiO_2 (3.2 eV; 388 nm). This fact points toward an influence of the FeO_x surface nanostructures and the presence of Ti(III) sites on the effective band gap of the system, since the band gap of Fe_3O_4 NPs is about 1.8–2.1 eV and that of reduced TiO_2 is $<$2.8 eV [82,83] NrGO is expected to act as a photosensitizer lowering the overall band gap energy (see Fig. S7). This is remarkably observed in PC-sws / PC-pn photocatalysts, which effectively exhibit the lowest GAP 1 of ca. 1.2–1.3 eV (954–1033 nm) values, whereas PC-sg / PC-pg reveal less remarkable change of the band gap as compared to TiO_2-FeO_x NPs (GAP 1: 2.1–2.2 eV, GAP 2: 3.0–3.2 eV). Noteworthy, these photocatalysts contain the least reduced NrGO structure (Fig. 5b-inset) and the largest

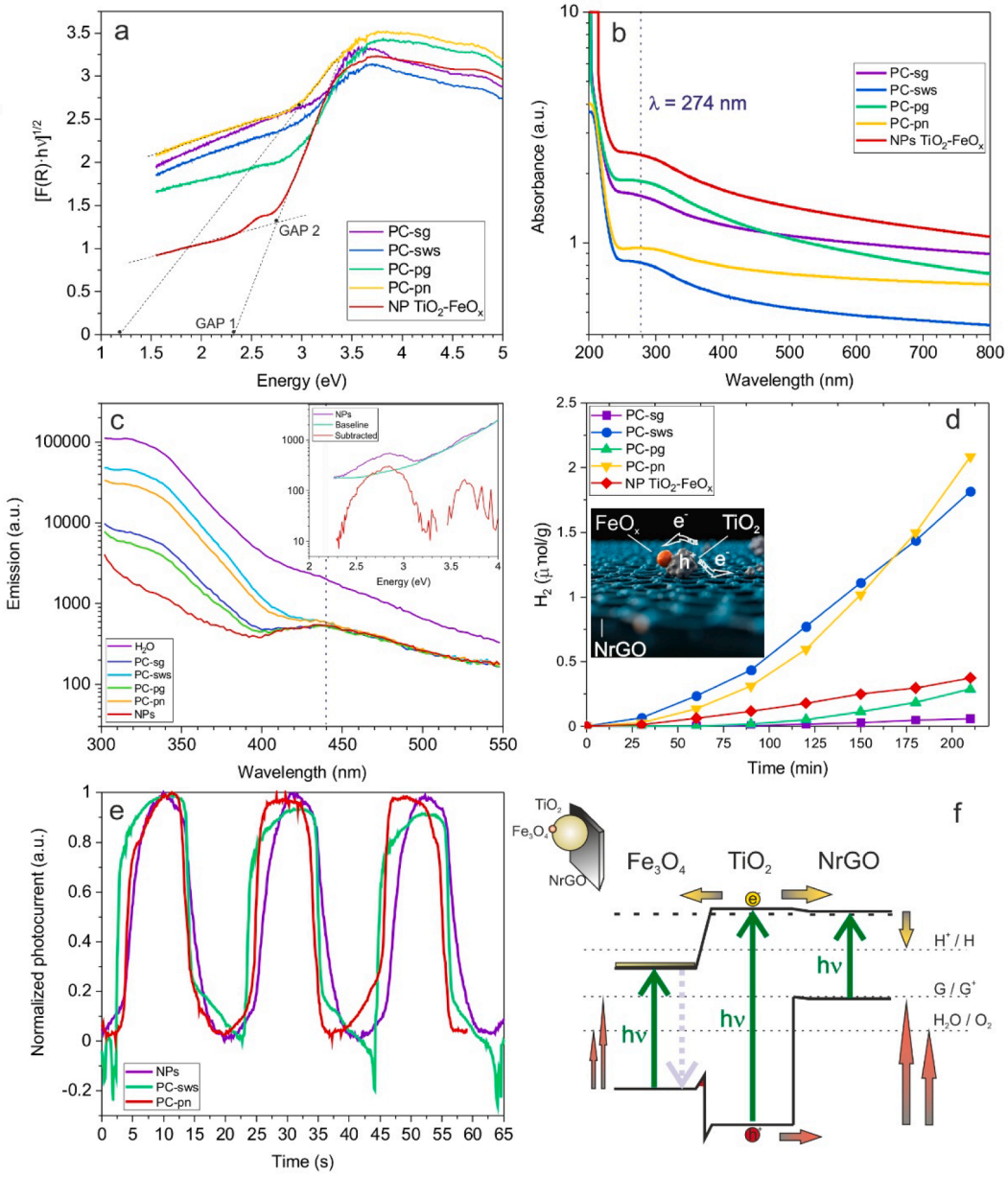

Fig. 6. (a) Tauc plots, (b) absorbance, (c) photoluminescence (λ_{exc}= 274 nm), (d) H_2 production of the developed photocatalysts as well as TiO_2-FeO_x NPs, (e) transient photocurrent measurements of PC-sws/PVA, PC-pn/PVA as well as TiO_2-FeO_x NPs/PVA films, and (f) schematic diagram of the photocatalytic mechanism. Insets: (c) Photoemission, baseline and subtracted component of NPs, (d) illustration of the proposed charge transport mechanism across the components of the photocatalysts.

Table 2
Calculated band gap energy values and H_2 production rate constant (0th order; k_0) of the photocatalysts and TiO_2-FeO_x NPs.

Sample	GAP 1 (eV)	GAP 2 (eV)	k_0 (nmol/g·min^2)
PC-sg	2.1	3.2	0.47±0.04
PC-sws	1.3	3.0	12.0 ± 0.2
PC-pg	2.2	3.0	2.3 ± 0.2
PC-pn	1.2	3.0	15±0.8
TiO_2-FeO_x NPs	2.3	2.7	2.0 ± 0.8

Ti(IV)/Ti(III) ratio.

It is worth noting that the optical behaviour of the photocatalysts can substantially change when present in dispersions. Therefore, additional studies were performed using 1 mg/mL aqueous dispersions of the NrGO-TiO_2-FeO_x photocatalysts and TiO_2-FeO_x NPs. Fig. 6b shows the absorbance spectra of the dispersions, which exhibit a very strong absorption at ca. 200 nm and a broader peak at approximately 270–280 nm. The absorbance signal increases from the sws to the pn, sg, and pg photocatalysts, revealing the highest absorption in the TiO_2-FeO_x NPs. Water was taken as the reference in the measurements, and it does not remarkably absorb radiation in the range of the spectrum around 270 nm, [84] so this broad peak can be ascribed to the TiO_2-FeO_x NPs. No additional bands related to the estimated band gap values were detected. This fact and the high absorbance levels at long wavelengths prompted us to consider the presence of light-scattering effects. Hence, the dispersions were analysed by DLS in two size ranges, nanometric and micrometric, using two different DLS equipment. The dispersions present a high polydispersity index in all cases, approximately 0.49 to 0.77, indicating a broad size distribution of the particles. On the other hand, it has to be considered that DLS provides a "hydrodynamic" size distribution, which is very sensitive to several factors as the shape (very

important in our case), internal motion of the particles, charge, concentration, sedimentation, etc. Therefore, the results must be used only for qualitative comparisons between the samples. Fig. S15a exhibits a very similar distribution of particles in the 1 – 10,000 nm range, centred at approximately 120 nm. However, the volume of the particles indeed shows a trimodal distribution centred at ca. 150, 770, and 5500 nm (Fig. S15b). As the DLS equipment used for the nanometric range presents technical limitations in the micrometric range, a more robust measurement of the volume distribution in the micrometric size range was acquired with a second equipment (Fig. S15c), revealing a broad distribution of particles in the 1–1000 μm range. The TiO_2-FeO_x NPs and PC-pg photocatalyst exhibit a distribution with smaller particles compared to the other photocatalysts. In summary, it can be assumed that the dispersions are composed of a similar distribution of mixed particles: the main component, about of tens to hundreds of nanometres in size, probably composed of TiO_2-FeO_x NPs and their aggregates (see Fig. S15a-inset), and micrometric to sub-millimetric aggregates mainly constituted by NrGO-TiO_2-FeO_x (see Fig. S15b-inset). The size distribution may change in real applications, since dynamic movement of the dispersion is made inside the reactor for extracting the H_2 gas and avoiding particle sedimentation.

Photoluminescence (PL) analyses were also performed in the aqueous dispersions using an excitation wavelength of 274 nm (Fig. 6c). The signal of liquid water was also acquired, revealing a broad band in the 300–400 nm range, which continue to decrease up to 550 nm. As water does not absorb 274 nm radiation, this signal is attributed to the fluorescence of the plastic recipient (microplate). The signals of the NrGO-TiO_2-FeO_x photocatalysts and TiO_2-FeO_x NPs are similar, but the 300–400 nm band intensity progressively decreases from sws photocatalyst to pn, sg, pg, and finally NPs, revealing the presence of a band at about 440 nm. This order of the signal intensity decrease coincides with that of the optical absorption increase (Fig. 6b), so it can be attributed to an increase in light scattering (note that PC-pg and TiO_2-FeO_x NPs somehow display the distributions of aggregates with smaller sizes; Fig. S15c). Therefore, UV light-scattering mechanisms are of substantial importance in the photocatalyst dispersions. A baseline was subtracted from the TiO_2-FeO_x NPs PL signal, which exhibited two emission bands (also present in the NrGO-TiO_2-FeO_x photocatalysts), one centred at ca. 2.8 eV attributed to shallow trap levels, and a very weak band centred at about 3.7 eV assigned to a direct X1b→X2b transition in TiO_2 (Fig. 6c-inset) [85] Note that 2.8 eV energy practically coincides with the estimated GAP 2 value of TiO_2-FeO_x NPs, confirming the presence of transitions to trap levels in both solid state and in aqueous dispersions. No emissions from the NrGO material were detected, probably because of their weakness.

The H_2 production yield of the synthetized photocatalysts was studied under UVA light radiation, using the sample of TiO_2-FeO_x NPs as a reference material. As observed in Fig. 6d, the NPs disclose a steady increase of the H_2 production with time up to a maximum of 0.38 μmol/g of H_2 at 210 min. Remarkably, the results obtained with the NrGO-TiO_2-FeO_x photocatalysts synthetized with the same laser conditions reveal significant functional differences, pointing towards a high influence of the structure of the system [15,34,86] PC-sg / PC-pg photocatalysts produce less amount of H_2 than the metal oxide NPs, 0.06 and 0.29 μmol/g at 210 min, respectively. However, PC-sws / PC-pn generate much higher amount of H_2 than the NPs, about 1.8 and 2.1 μmol/g at 210 min, respectively. It has to be noticed that the photocatalysts exhibiting the highest production yield are the ones revealing the smallest band gap energy (Fig. 6a, Table 2) and the lowest light scattering mechanisms (Fig. 6b, c), pointing toward a direct relation between these magnitudes. Another feature to consider is that, even though the initial kinetics seem to be slow, the H_2 production of the NrGO-TiO_2-FeO_x photocatalysts and TiO_2-FeO_x NPs increases linearly in time afterwards. Then, the H_2 production can be classified as a classical 0th order reaction (rate reaction not dependent on the reactants concentration), and the H_2 production rate constant can be calculated (Table 2). As expected, the PC-sws / PC-pn photocatalysts show significantly higher H_2 production rate constant than the rest of systems, being PC-sg (exhibiting disrupted NrGO structure) the worst. Furthermore, an additional characterization (not shown) of a sample obtained by physical mixing NrGO-sws sheets (1st irradiation step) and TiO_2-FeO_x NPs (2nd irradiation step developed without NrGO sheets) did not produce relevant amount of H_2, highlighting the importance of fixing the semiconducting nanostructures to the NrGO sheets. Transient photocurrent measurements were also taken in films of PC-sws and PC-pn photocatalysts, as well as TiO_2-FeO_x NPs mixed with PVA (binder) and deposited on FTO glass substrates. After a few minutes of stabilization, the generated photocurrent of all the samples displayed the typical pulsed profile due to the periodic on-off light cycles (Fig. 6e). The average FWHM pulse duration is 9.8 ± 0.2, 11.6 ± 0.5, and 9.3 ± 0.1 s in TiO_2-FeO_x NPs, PC-sws and PC-pn, respectively. As observed, the steps are not abrupt, and no "on" overshoots are observed in any of the samples, whereas only PC-sws shows "off" spikes. The long rise time of the photocurrent and the absence of overshoots would indicate a high recombination rate. Moreover, the negative overshoot seen after light switching off in PC-sws would reveal a slow decay of the excess of holes by recombination and charge transfer [87]. This fact might indicate an effective separation of electron and holes during the photocatalyst illumination. Note that PC-sws is the photocatalyst with the highest amount of graphitic nitrogen. It is also worth mentioning that the presence of PVA ligand might increase the resistance of the material, and hence, the time constant of the transient processes. Besides, some additional photochemical processes could arise under the interaction between the photocatalysts and the PVA material submitted to intense UV light.

EIS characterization of the films composed of PC-sws/PVA and PC-pn/PVA photocatalysts, as well as TiO_2-FeO_x NPs/PVA was performed in dark conditions (Fig. S16). A modified Randles cell equivalent circuit, containing resistors, as well as a constant phase and a Warburg elements was proposed for fitting the Nyquist curves. As observed in Table S1, the equivalent series resistance of the film containing the TiO_2-FeO_x NPs is higher than that of PC-sws and PC-pn, due to the conducting nature of the NrGO sheets. Moreover, the charge transfer resistance and Warburg coefficients of the TiO_2-FeO_x NPs film are considerably higher than those of PC-sws and PC-pn, accounting for an enhancement of the chemical reactivity and diffusivity upon the addition of the NrGO material to the semiconducting NPs. On the other hand, the Mott-Schottky analysis reveals the expected n type nature of the TiO_2-FeO_x NPs film in almost all the potential range, similarly to the behaviour of PC-pn. However, PC-sws shows a more complex p and n type nature in different potential regions. The noisy behaviour of PC-sws and PC-pn measurements, not visible in the TiO_2-FeO_x NPs film, could be indicative of electrochemical interactions between the NrGO structures and the PVA / electrolyte. The flat band potential of the films, determined through linear fitting of the plots in the n type regions indicated in the inset of Fig. S16, reveals similar values of −1.1 ± 0.1 V and −1.0 ± 0.3 V for TiO_2-FeO_x NPs and PC-pn films, respectively, and −2.1 ± 1.1 V for PC-sws. From the values of the slope, it can be concluded that the carrier density of all the samples is very similar, being determined by the TiO_2-FeO_x NPs.

The photocatalytic H_2 production mechanism of FeO_x-decorated TiO_2 NPs coating NrGO flakes under UV light involves several key steps, driven by the interaction between FeO_x, TiO_2, and NrGO [88,89] Based on the literature about the structural components of the photocatalysts, an overall photoreforming process can be proposed. The expected energy band structure after the formation of the NrGO-TiO_2-FeO_x junctions is explained in the Section 6 of SM (Fig. S17, Table S2). Upon UV illumination, FeO_x-TiO_2 NPs (acting as the primary photocatalyst) absorb the photons with energy greater than or equal to their band gap, creating electron-hole pairs (e^-/h^+) (Fig. 6f). Note that the presence of Ti(III) sites, not considered in the scheme, would create interstitial states in the band gap allowing the absorption of lower energy photons in the TiO_2 material [73]. The narrower band gap of FeO_x (mainly Fe_3O_4) compared

to TiO_2, combined with the presence of an interfacial potential barrier in the valence band (VB) might act as a charge separator in the FeO_x-TiO_2 composite. However, the trapped photogenerated electrons from the TiO_2 conduction band (CB) in the FeO_x nanostructures cannot participate in the reduction of protons (H^+) in water, due to the higher CB energy than the proton reduction potential, leading to an increase of the e^-/h^+recombination rate. Therefore, only the remaining electrons in the TiO_2 CB can lead to hydrogen generation ($2H^+ + 2e^- \rightarrow H_2$), and the holes left in the TiO_2 VB participate in the oxidation of water and glycerol [90]. To the contrary, just a negligible portion of holes from the Fe_3O_4 would participate in this process. Small fraction of Fe_2O_3, if exists, would not participate in the reduction of protons due to its CB energy [91] The glycerol decomposition contributes to the generation of hydrogen and carbon dioxide ($C_3H_8O_3 + 3H_2O \rightarrow 3CO_2 + 7H_2$) [92,93] In the NrGO-$TiO_2$-$FeO_x$ photocatalysts, N-doped rGO constituted by p-n type heterojunctions, would also absorb photons contributing with e^-/h^+ carriers and, with its excellent conductivity and nitrogen-doped active sites, serves as an electron acceptor (Fig. 6f-inset) [22,23] Accordingly, part of the electrons created in TiO_2 are transferred to the NrGO layer, where they are delocalized across the graphene domains, preventing e^-/h^+ recombination. However, due to the slight CB energy difference between TiO_2 and NrGO, the capability of extraction of electrons from TiO_2 will extremely depend on the type and number of N-doping groups (i.e. position of Fermi level). Evidently, the efficiency of the hydrogen generation process depends on the combined effects of extended light absorption range, enhanced charge separation, density of structural defects that can act as recombination centers, and effective catalytic sites provided by NrGO. Besides, the quantity of light arriving to the photocatalysts surface is crucial. Consequently, PC-sws/PC-pn exhibit the largest H_2 production yield due to their reduced GO structure, allowing the π-bonding conjugation and moderate N-doping (especially with graphitic N), and enhancing electron affinity and charge carriers' separation, as well as their augmented optical absorbance (lowest band gap) and lesser light-scattering nature. Contrarily, PC-sg/PC-pg photocatalysts reveal lower optical absorbance (highest band gap), which produces less amount of e^-/h^+ pairs, as well as the presence of larger quantity of C—O moieties and a small amount of titanium carbide, which might contribute to the carriers' recombination. This effect is especially important in PC-sg photocatalyst, which NrGO structure is seriously damaged by the laser irradiation process, leading to a scarce H_2 generation yield. These two photocatalysts also exhibit larger light-scattering effects, which seriously limit the amount of radiation reaching the particles surface. Finally, stability studies of the PC-sws photocatalyst (Fig. S18) revealed a decrease of approximately 50 % in the H_2 yield in subsequent runs, indicating a notable reduction of reactivity. Future studies should focus on maximizing the H_2 production and photocatalyst stability. The great versatility of the liquid-assisted laser irradiation technique should allow functional optimization by tuning experimental parameters such as the precursor concentration, laser fluence, laser wavelength, and number of accumulated pulses.

4. Conclusion

The liquid phase irradiation of precursor dispersions has been demonstrated as a highly versatile and powerful technology for the simple synthesis of complex hybrid photocatalysts. The extreme thermodynamic conditions that the precursor components experience upon the UV laser pulses allow obtaining highly crystalline TiO_2-FeO_x nanostructures coating N-doped reduced GO sheets. Besides, the initial thickness and chemical composition of the GO sheet precursor has been revealed as key factors, determining the reaction pathway and final configuration of the photocatalyst. The H_2 production does not depend on a unique feature of the composite, but on a holistic activity of different structural components. An excess of C—OH groups in GO-sg provokes its high reactivity with imidazole, resulting in the substantial degradation of the NrGO material, which blocks the H_2 production of TiO_2-FeO_x nanostructures. GO-pn, GO-pg, and GO-sws precursors show similar relative amount of chemical groups but, after the synthetic process, produce composites with significantly different optical properties and H_2 production yields, pointing to complex reaction paths also influenced by the sheets thickness (i. e. developed temperatures). The compositional studies indicate that a high reduction degree with a moderate concentration of C—OH groups, as well as a low concentration of sulphur in the GO structure leads to a better performance in the final photocatalyst. The greatest H_2 production yield is obtained in PC-sws/PC-pn photocatalysts, which are characterized by the highest concentration of $C = C$ (sp^2), graphitic N groups, and Ti (III) sites in TiO_2. These composites exhibit the presence of 4–6 at.% of N. In contrast, the worst photocatalysts (PC-sg/PC-pg) are characterized by much higher concentration of N sites (> 13 at.%), probably enabling a high structural disruption, the presence of TiC and the lowest concentration of Ti(III) sites. Surface FeO_x (mainly Fe_3O_4) nanocrystals on TiO_2 allow reducing the optical band gap to 2.3 – 2.7 eV but induces charge recombination, whereas PC-sws/PC-pn exhibit a further optical band gap reduction to ca. 1.2–3.0 eV due to the presence of NrGO and a higher amount of Ti (III) sites in TiO_2. The greater H_2 production yield of these photocatalysts is directly related to their lower band gap, which increases the generation of excitons, as well as high reduction and moderate N-doping (especially with graphitic and pyridinic N) of NrGO, which enhances the e^-/h^+ separation and reactivity for the water splitting process. Finally, it has to be noted the remarkable light-scattering nature that the photocatalysts exhibit in the UV range, which considerably limits the amount of radiation arriving inside the dispersion. This effect is more pronounced in the photocatalysts showing the least H_2 production yield. Although the H_2 yield is modest, this work demonstrates a scalable synthesis route and highlights the critical role of GO precursors, paving the way for optimization.

CRediT authorship contribution statement

María Susana Gutiérrez: Writing – review & editing, Methodology, Investigation. **José Peral:** Writing – review & editing, Methodology, Investigation, Formal analysis. **Dominique Buyens:** Writing – review & editing, Methodology. **Enikö György:** Writing – review & editing, Validation, Supervision, Project administration, Funding acquisition, Formal analysis, Data curation, Conceptualization. **Ángel Pérez del Pino:** Writing – original draft, Visualization, Validation, Supervision, Resources, Project administration, Methodology, Investigation, Funding acquisition, Formal analysis, Data curation, Conceptualization.

Declaration of competing interest

The authors declare the following financial interests/personal relationships which may be considered as potential competing interests:

Angel Perez del Pino reports financial support was provided by Spanish Scientific Research Council. If there are other authors, they declare that they have no known competing financial interests or personal relationships that could have appeared to influence the work reported in this paper.

Acknowledgments

The authors thank the financial support through the grant TED2021–130477B-I00 funded by MCIN/AEI/10.13039/501100011033 and by the European Union NextGeneration EU/PRTR, as well as the grants CEX2023–001263-S from the State Investigation Agency, through Severo Ochoa Program for Centers of Excellence in R&D, and 2022 SGR 0936 from AGAUR of Generalitat de Catalunya. This project also received funding from the European Union's Horizon 2020 research and innovation programme, under the grant agreement No 101007417 NFFA-Europe Pilot (project ID 476), having benefited from the access provided by the SIAM platform at the University of

Namur for XPS characterization, and Karlsruhe Institute of Technology, Institute of Microstructure Technology installations, for NMR analyses. The authors also acknowledge the support of Graphenea, Salvador Bartolomé (Fluorescence spectroscopy service of UAB), the scientific-technical and prototyping services of ICMAB (particularly, to Amable Bernabé, Xavier Rodriguez, and Gerard Albujer), as well as Rachel Gouttenbaron (SIAM) to this research.

Supplementary materials

Supplementary material associated with this article can be found, in the online version, at doi:10.1016/j.materresbull.2025.113899.

Data availability

Data will be made available on request.

References

[1] N. M. Santhosh, G. Filipič, E. Kovacevic, A. Jagodar, J. Berndt, T. Strunskus, H. Kondo, M. Hori, E. Tatarova, U. Cvelbar, N-graphene nanowalls via plasma nitrogen incorporation and substitution: the experimental evidence, Nano-Micro Lett. 12 (1) (2020) 12–53, https://doi.org/10.1007/s40820-020-0395-5.

[2] R.H. Lin, Y.Y. Zhao, B.D. Wu, Toward a Hydrogen Society: hydrogen and smart grid integration, Int. J. Hydrogen Energy 45 (39) (2020) 20164–20175, https://doi.org/10.1016/J.IJHYDENE.2020.01.047.

[3] A. Raveendran, M. Chandran, R. Dhanusuraman, A comprehensive review on the electrochemical parameters and recent material development of electrochemical water splitting electrocatalysts, RSC Adv. 13 (6) (2023) 3843–3876.

[4] S.P. Shelake, D.N. Sutar, B.M. Abraham, T. Banerjee, A.V.S. Sainath, U. Pal, Emerging photoreforming process to hydrogen production: a future energy, Adv. Funct. Mater. (40) (2024) 34, https://doi.org/10.1002/adfm.202403795.

[5] H. Zhao, J. Liu, N. Zhong, S. Larter, Y. Li, M.G. Kibria, B. Su, Z. Chen, J. Hu, Biomass photoreforming for hydrogen and value-added chemicals Co-production on hierarchically porous photocatalysts, Adv. Energy Mater. (21) (2023) 13, https://doi.org/10.1002/aenm.202300257.

[6] N. Fajrina, M. Tahir, A critical review in strategies to improve photocatalytic water splitting towards hydrogen production, Int. J. Hydrogen Energy 44 (2) (2019) 540–577, https://doi.org/10.1016/J.IJHYDENE.2018.10.200.

[7] T.-Y. Shuai, Q.-N. Zhan, H.-M. Xu, Z.-J. Zhang, G.-R. Li, Recent developments of MXene-based catalysts for hydrogen production by water splitting, Green Chem 25 (5) (2023) 1749–1789, https://doi.org/10.1039/D2GC04205C.

[8] X. Tao, Y. Zhao, S. Wang, C. Li, R. Li, Recent advances and perspectives for solar-driven water splitting using particulate photocatalysts, Chem. Soc. Rev. 51 (9) (2022) 3561–3608, https://doi.org/10.1039/D1CS01182K.

[9] R. Mishra, S. Bera, R. Chatterjee, S. Banerjee, S. Bhattacharya, A. Biswas, S. Mallick, S. Roy, A review on Z/S – Scheme heterojunction for photocatalytic applications based on metal halide perovskite materials, Appl. Surf. Sci. Adv. 9 (2022) 100241, https://doi.org/10.1016/J.APSADV.2022.100241.

[10] P. Ganguly, M. Harb, Z. Cao, L. Cavallo, A. Breen, S. Dervin, D.D. Dionysiou, S. C. Pillai, 2D Nanomaterials for photocatalytic hydrogen production, ACS Energy Lett. 4 (7) (2019) 1687–1709, https://doi.org/10.1021/ACSENERGYLETT.9B00940/ASSET/IMAGES/LARGE/NZ-2019-00940Y_0020.JPEG.

[11] S. Zhan, Y. Yang, L. Taixu, A. Sanja, W. Lin, H. Huilin, T. Nengrong, L. Pengcheng, L. Weijun, Y. Weiyou, 0D/2D Heterojunction photocatalysts for improved full-spectrum-light-driven hydrogen evolution, J. Mater. Chem. A 12 (42) (2024) 29278–29287, https://doi.org/10.1039/D4TA06179A.

[12] S.K. Lakhera, K.P. Kangeyan, C. Yazhini S, S. Golda A, N. Bernaurdshaw, Advances in hybrid strategies for enhanced photocatalytic water splitting: bridging conventional and emerging methods, Appl. Phys. Rev. 11 (4) (2024) 41305, https://doi.org/10.1063/5.0218539.

[13] A. Ali, S.U.H. Bakhtiar, A. Ismail, P.M. Ismail, S. Hayat, A. Zada, X. Wu, A. N. Alodhayb, M. Zahid, F. Raziq, J. Yi, L. Q. Transition metal sulfides: from design strategies to environmental and energy-related applications, Coord. Chem. Rev. 523 (1) (2025) 216237, https://doi.org/10.1016/j.ccr.2024.216237.

[14] M. Chu, H. Ma, Z. Liu, X. Jiang, N. Kang, X. Liu, G. Xie, Template-synthesized CdWO4/Cd0.5Zn0.5S hollow microsphere photocatalyst for high-efficient hydrogen evolution under visible light, Int. J. Hydrogen Energy 90 (2024) 874–884, https://doi.org/10.1016/J.IJHYDENE.2024.10.034.

[15] B. Kakavandi, M. Moradi, F. Hasanvandian, A. Bahadoran, E. Mohebolkhames, M. Golshan, S. Ganachari, T.M. Aminabhavi, Visible light-assisted S-scheme p- and n-type semiconductors anchored onto graphene for increased photocatalytic H2 production via water splitting, Chem. Eng. J. 487 (2024) 150399, https://doi.org/10.1016/j.cej.2024.150399.

[16] M. Ismael, A review and recent advances in solar-to-hydrogen energy conversion based on photocatalytic water splitting over doped-TiO2 nanoparticles, Sol. Energy 211 (2020) 522–546, https://doi.org/10.1016/J.SOLENER.2020.09.073.

[17] F. Bhom, Y.M. Isa, Photocatalytic hydrogen production using TiO 2 -based catalysts: a review, Glob. Challenges 8 (11) (2024), https://doi.org/10.1002/gch2.202400134.

[18] M.S. Reza, N.B.H. Ahmad, S. Afroze, J. Taweekun, M. Sharifpur, A.K. Azad, Hydrogen production from water splitting through photocatalytic activity of carbon-based materials, Chem. Eng. Technol. 46 (3) (2023) 420–434, https://doi.org/10.1002/ceat.202100513.

[19] C.S. Bongu, S. Tasleem, M.R. Krishnan, E.H. Alsharaeh, Graphene-based 2D materials for rechargeable batteries and hydrogen production and storage: a critical review, Sustain. Energy Fuels 8 (18) (2024) 4039–4070, https://doi.org/10.1039/D4SE00497C.

[20] A. Mondal, A. Prabhakaran, S. Gupta, V.R. Subramanian, Boosting photocatalytic activity using reduced graphene oxide (RGO)/semiconductor nanocomposites: issues and future scope, ACS Omega 6 (13) (2021).

[21] J. Corredor, M.J. Rivero, I. Ortiz, New insights in the performance and reuse of RGO/TiO2 composites for the photocatalytic hydrogen production, Int. J. Hydrogen Energy 46 (33) (2021) 17500–17506, https://doi.org/10.1016/J.IJHYDENE.2020.01.181.

[22] X. Li, R. Shen, S. Ma, X. Chen, J. Xie, Graphene-based heterojunction photocatalysts, Appl. Surf. Sci. 430 (2018) 53–107, https://doi.org/10.1016/j.apsusc.2017.08.194.

[23] H. Wang, T. Maiyalagan, X. Wang, Review on recent progress in nitrogen-doped graphene: synthesis, characterization, and its potential applications, ACS Catal 2 (5) (2012) 781–794, https://doi.org/10.1021/CS200652Y.

[24] T.-F. Yeh, C.-Y. Teng, S.-J. Chen, H. Teng, T. Yeh, C. Teng, H. Teng, S. Chen, Nitrogen-doped graphene oxide quantum dots as photocatalysts for overall water-splitting under visible light illumination, Adv. Mater. 26 (2014) 3297–3303, https://doi.org/10.1002/adma.201305299.

[25] M. Humayun, C. Wang, W. Luo, Recent progress in the synthesis and applications of composite photocatalysts: a critical review, Small Methods 6 (2) (2022) 2101395, https://doi.org/10.1002/smtd.202101395.

[26] R. Mahdavi, S.S.A. Talesh, Sol-gel synthesis, structural and enhanced photocatalytic performance of Al doped ZnO nanoparticles, Adv. Powder Technol. 28 (5) (2017) 1418–1425, https://doi.org/10.1016/J.APT.2017.03.014.

[27] J. Yang, X. Wu, Z. Mei, S. Zhou, Y. Su, G. Wang, J. Yang, X. Wu, Z. Mei, G. Wang, S. Zhou, Y. Su, CVD assisted synthesis of macro/mesoporous TiO2/g-C3N4 S-scheme heterojunction for enhanced photocatalytic hydrogen evolution, Adv. Sustain. Syst. 6 (8) (2022) 2200056, https://doi.org/10.1002/ADSU.202200056.

[28] R. Ivan, C. Popescu, A.P. del Pino, I. Yousef, C. Logofatu, E. György, Laser-induced synthesis and photocatalytic properties of hybrid organic–Inorganic composite layers, J. Mater. Sci. 54 (5) (2019) 3927–3941, https://doi.org/10.1007/s10853-018-3144-0.

[29] A. Queraltó, E. György, R. Ivan, Á.P. Del Pino, R. Frohnhoven, S. Mathur, Enhanced UV-vis photodegradation of nanocomposite reduced graphene oxide/ferrite nanofiber films prepared by laser-assisted evaporation, Crystals 10 (4) (2020) 271, https://doi.org/10.3390/cryst10040271.

[30] R. Ivan, A. Pérez del Pino, I. Yousef, C. Logofatu, E. György, Laser synthesis of TiO2–Carbon nanomaterial layers with enhanced photodegradation efficiency towards antibiotics and dyes, J. Photochem. Photobiol. A Chem. 399 (2020) 112616, https://doi.org/10.1016/J.JPHOTOCHEM.2020.112616.

[31] V. Amendola, D. Amans, Y. Ishikawa, N. Koshizaki, S. Scirè, G. Compagnini, S. Reichenberger, S. Barcikowski, Room-temperature laser synthesis in liquid of oxide, metal-oxide core-shells, and doped oxide nanoparticles, Chem. – A Eur. J 26 (42) (2020) 9206–9242, https://doi.org/10.1002/chem.202000686.

[32] J. Theerthagiri, K. Karuppasamy, S.J. Lee, R. Shwetharani, H.-S. Kim, S.K.K. Pasha, M. Ashokkumar, M.Y. Choi, Fundamentals and comprehensive insights on pulsed laser synthesis of advanced materials for diverse photo- and electrocatalytic applications, Light Sci. Appl. 11 (1) (2022) 250, https://doi.org/10.1038/s41377-022-00904-7.

[33] S.S. Naik, S.J. Lee, T. Begildayeva, Y. Yu, H. Lee, M.Y. Choi, Pulsed laser synthesis of reduced graphene oxide supported ZnO/Au nanostructures in liquid with enhanced solar light photocatalytic activity, Environ. Pollut. 266 (2020) 115247, https://doi.org/10.1016/j.envpol.2020.115247.

[34] A. Pérez del Pino, A. González-Campo, S. Giraldo, J. Peral, E. György, C. Logofatu, A.J. deMello, J. Puigmartí-Luis, Synthesis of graphene-based photocatalysts for water splitting by laser-induced doping with ionic liquids, Carbon 130 (2018) 48–58, https://doi.org/10.1016/j.carbon.2017.12.116.

[35] R.C. Forsythe, C.P. Cox, M.K. Wilsey, A.M. Müller, Pulsed laser in liquids made nanomaterials for catalysis, Chem. Rev. 121 (13) (2021) 7568–7637, https://doi.org/10.1021/acs.chemrev.0c01069.

[36] P. Makuła, M. Pacia, W. Macyk, How to correctly determine the band gap energy of modified semiconductor photocatalysts based on UV–Vis spectra, J. Phys. Chem. Lett. 9 (23) (2018) 6814–6817, https://doi.org/10.1021/acs.jpclett.8b02892.

[37] R. Ivan, C. Popescu, V.A. Antohe, S. Antohe, C. Negrila, C. Logofatu, A.P. del Pino, E. György, Iron oxide/hydroxide–Nitrogen doped graphene-like visible-light active photocatalytic layers for antibiotics removal from wastewater, Sci. Rep. 13 (1) (2023) 2740, https://doi.org/10.1038/s41598-023-29927-9.

[38] S.M. Omalley, J. Tomko, A.P.D. Pino, C. Logofatu, E. György, Resonant infrared and ultraviolet matrix-assisted pulsed laser evaporation of titanium oxide/graphene oxide composites: a comparative study, J. Phys. Chem. C 118 (48) (2014), https://doi.org/10.1021/jp509067u.

[39] Á.P.Del Pino, E. György, C. Logofatu, A. Duta, Study of the deposition of graphene oxide by matrix-assisted pulsed laser evaporation, J. Phys. D. Appl. Phys. 46 (2013) 505309, https://doi.org/10.1088/0022-3727/46/50/505309.

[40] İ. Dinçer, C. Zamfirescu, Drying phenomena: theory and applications, Dry. Phenom. Theory Appl. (2015) 1–482, https://doi.org/10.1002/9781118534892.

[41] I. Fleming, D. Williams, Spectroscopic Methods in Organic Chemistry, Springer International Publishing: Cham, 2019, https://doi.org/10.1007/978-3-030-18252-6.

[42] D.R. Dreyer, S. Park, C.W. Bielawski, R.S. Ruoff, The chemistry of graphene oxide, Chem. Soc. Rev. (2010) 228–240, https://doi.org/10.1039/b917103g.

[43] Á. Pérez del Pino, M.A. Ramadan, P. Garcia Lebière, R. Ivan, C. Logofatu, I. Yousef, E. György, Fabrication of graphene-based electrochemical capacitors through reactive inverse matrix assisted pulsed laser evaporation, Appl. Surf. Sci. 484 (2019) 245–256, https://doi.org/10.1016/j.apsusc.2019.04.127.

[44] P. García Lebière, Á. Pérez Del Pino, G.D. Domingo, C. Logofatu, I. Martínez-Rovira, I. Yousef, E. György, Laser fabrication of hybrid electrodes composed of nanocarbons mixed with cerium and manganese oxides for supercapacitive energy storage, J. Mater. Chem. A 9 (2) (2021) 1192–1206, https://doi.org/10.1039/D0TA06756C.

[45] P. García Lebière, A. Pérez del Pino, C. Logofatu, E. György, Laser synthesis of NixZnyO/reduced graphene oxide/carbon nanotube electrodes for energy storage applications, Appl. Surf. Sci. 563 (2021) 150234, https://doi.org/10.1016/J.APSUSC.2021.150234.

[46] Y. Sun, C. Li, G. Shi, Nanoporous nitrogen doped carbon modified graphene as electrocatalyst for oxygen reduction reaction, J. Mater. Chem. 22 (25) (2012) 12810, https://doi.org/10.1039/c2jm31525d.

[47] S. Sandoval, N. Kumar, J. Oro-Solé, A. Sundaresan, C.N.R. Rao, A. Fuertes, G. Tobias, Tuning the nature of nitrogen atoms in N-containing reduced graphene oxide, Carbon 96 (2016) 594–602, https://doi.org/10.1016/j.carbon.2015.09.085.

[48] I.L. Malaestean, M. Kutluca-Alıcı, A. Ellern, J. van Leusen, H. Schilder, M. Speldrich, S.G. Baca, P.Linear Kögerler, Zigzag, and helical cerium(III) coordination polymers, Cryst. Growth Des. 12 (3) (2012) 1593–1602, https://doi.org/10.1021/cg2016337.

[49] Properties of atoms, radicals, and bonds https://labs.chem.ucsb.edu/zakarian/armen/11—bonddissociationenergy.pdf.

[50] S.J. Blanksby, G.B. Ellison, Bond dissociation energies of organic molecules, Acc. Chem. Res. 36 (4) (2003) 255–263, https://doi.org/10.1021/ar020230d.

[51] A. Vogel, V. Venugopalan, Mechanisms of pulsed laser ablation of biological tissues, Chem. Rev. 103 (2) (2003) 577–644, https://doi.org/10.1021/cr010379n.

[52] P.E. Dyer, J. Sidhu, Excimer laser ablation and thermal coupling efficiency to polymer films, J. Appl. Phys. 57 (4) (1985) 1420–1422, https://doi.org/10.1063/1.334503.

[53] B.I. Costescu, I.B. Baldus, F. Gräter, Graphene mechanics: I. Efficient first principles based morse potential, Phys. Chem. Chem. Phys. 16 (24) (2014) 12591–12598, https://doi.org/10.1039/C3CP55340J.

[54] D. Kepić, S. Sandoval, Á.P.del Pino, E. György, L. Cabana, B. Ballesteros, G. Tobias, Nanosecond laser-assisted nitrogen doping of graphene oxide dispersions, ChemPhysChem 18 (8) (2017) 935–941, https://doi.org/10.1002/cphc.201601256.

[55] A. Watanabe, T. Tsuchiya, Y. I, Selective deposition of anatase and rutile films by KrF laser chemical vapor deposition from titanium isopropoxide, Thin Solid Films 406 (1–2) (2002) 132–137.

[56] K.S. Ershov, S.A. Kochubei, V.G. Kiselev, A.V. Baklanov, Decomposition pathways of titanium isopropoxide Ti(O i Pr) 4 : new insights from UV-photodissociation experiments and quantum chemical calculations, J. Phys. Chem. A 122 (4) (2018) 1064–1070, https://doi.org/10.1021/acs.jpca.7b10396.

[57] N. Nagalingam, A. Raghunathan, V. Korede, C. Poelma, C.S. Smith, R. Hartkamp, J. T. Padding, H.B. Eral, Laser-induced cavitation for controlling crystallization from solution, Phys. Rev. Lett. 131 (12) (2023) 124001, https://doi.org/10.1103/PhysRevLett.131.124001.

[58] G. Sinibaldi, A. Occhicone, F. Alves Pereira, D. Caprini, L. Marino, F. Michelotti, C. M. Casciola, Laser induced cavitation: plasma generation and breakdown shockwave, Phys. Fluids 31 (10) (2019) 103302, https://doi.org/10.1063/1.5119794/1075989.

[59] T. Zhang, Z. Wang, D.J. Hwang, Metal oxide hollow nanoparticles formation by a single nanosecond pulsed laser ablation in liquid, Appl. Phys. A 123 (10) (2017) 616, https://doi.org/10.1007/s00339-017-1222-9.

[60] L. Wang, Y. Wu, X. Wu, K. C, Measurement of dynamics of laser-induced cavitation around nanoparticle with high-speed digital holographic microscopy, Exp. Therm. Fluid Sci. 121 (2021) 110266.

[61] C. Fan, C. Chen, J. Wang, X. Fu, Z. Ren, G. Qian, Z. Wang, B.lack hydroxylated titanium dioxide prepared via ultrasonication with enhanced photocatalytic activity, Sci. Rep. 5 (1) (2015) 11712, https://doi.org/10.1038/srep11712.

[62] S. Pei, H.M. Cheng, The reduction of graphene oxide, Carbon 50 (9) (2012) 3210–3228, https://doi.org/10.1016/J.CARBON.2011.11.010.

[63] R. Al-Gaashani, A. Najjar, Y. Zakaria, S. Mansour, M.A. Atieh, XPS and Structural studies of high quality graphene oxide and reduced graphene oxide prepared by different chemical oxidation methods, Ceram. Int. 45 (11) (2019) 14439–14448, https://doi.org/10.1016/J.CERAMINT.2019.04.165.

[64] G… Beamson, D. Briggs, High resolution XPS of organic polymers: the Scienta ESCA300 database (Beamson, G.; Briggs, D.), J. Chem. Educ. 70 (1) (1993), https://doi.org/10.1021/ed070pA25.5. A25.

[65] G.H. Major, N. Fairley, P.M.A. Sherwood, M.R. Linford, J. Terry, V. Fernandez, K. Artyushkova, Practical guide for curve fitting in X-ray photoelectron spectroscopy, J. Vac. Sci. Technol. A Vacuum Surf. Film. 38 (6) (2020) 61203, https://doi.org/10.1116/6.0000377/1023652.

[66] A. Carvalho, M.C.F. Costa, V.S. Marangoni, P.R. Ng, T.L.H. Nguyen, A.H. Castro Neto, The degree of oxidation of graphene oxide, Nanomaterials 11 (3) (2021) 560, https://doi.org/10.3390/NANO11030560.

[67] S.E. Shin, H.J. Choi, J.Y. Hwang, D. H. B. Strengthening behavior of carbon/metal nanocomposites, Sci. Rep. 5 (2015) 16114.

[68] M.C. Biesinger, L.W.M. Lau, A.R. Gerson, R.S.C Smart, Resolving surface chemical states in XPS analysis of first row transition metals, oxides and hydroxides: sc, Ti, V, Cu and Zn, Appl. Surf. Sci. 257 (3) (2010) 887–898, https://doi.org/10.1016/J.APSUSC.2010.07.086.

[69] S. Kavitha, R. Ranjith, N. Jayamani, S. Vignesh, B. Palanivel, R. Djellabi, C. L. Bianchi, F.A. Alharthi, Fabrication of visible-light-responsive TiO2/α-Fe2O3-heterostructured composite for rapid photo-oxidation of organic pollutants in water, J. Mater. Sci. Mater. Electron. 33 (11) (2022) 8906–8919, https://doi.org/10.1007/s10854-021-06971-7.

[70] R. Vishwakarma, G. Kalita, S.M. Shinde, Y. Yaakob, C. Takahashi, M. Tanemura, Structure of nitrogen-doped graphene synthesized by combination of imidazole and melamine solid precursors, Mater. Lett. 177 (2016) 89–93, https://doi.org/10.1016/j.matlet.2016.04.155.

[71] D. Nolting, N. Ottosson, M. Faubel, I.V. Hertel, B. Winter, Pseudoequivalent nitrogen atoms in aqueous imidazole distinguished by chemical shifts in photoelectron spectroscopy, J. Am. Chem. Soc. 130 (26) (2008) 8150–8151, https://doi.org/10.1021/JA8022384.

[72] S. Mohajernia, P. Andryskova, G. Zoppellaro, S. Hejazi, S. Kment, R. Zboril, J. Schmidt, P. Schmuki, Influence of Ti3+ defect-type on heterogeneous photocatalytic H2 evolution activity of TiO2, J. Mater. Chem. A 8 (3) (2020) 1432–1442, https://doi.org/10.1039/C9TA10855F.

[73] Z. Xiu, M. Guo, T. Zhao, K. Pan, Z. Xing, Z. Li, W. Zhou, Recent advances in Ti3+ self-doped nanostructured TiO2 visible light photocatalysts for environmental and energy applications, Chem. Eng. J. 382 (2020) 123011, https://doi.org/10.1016/j.cej.2019.123011.

[74] B. Bharti, S. Kumar, H.N. Lee, R. Kumar, Formation of oxygen vacancies and Ti3+ State in TiO2 thin film and enhanced optical properties by air plasma treatment, Sci. Reports 2016 61 6 (1) (2016) 1–12, https://doi.org/10.1038/srep32355.

[75] M.C. Biesinger, B.P. Payne, A.P. Grosvenor, L.W.M. Lau, A.R. Gerson, R.S.C Smart, Resolving surface chemical states in XPS analysis of first row transition metals, oxides and hydroxides: cr, Mn, Fe, Co and Ni, Appl. Surf. Sci. 257 (7) (2011) 2717–2730, https://doi.org/10.1016/j.apsusc.2010.10.051.

[76] A.P. Grosvenor, B.A. Kobe, M.C. Biesinger, N.S. McIntyre, Investigation of multiplet splitting of Fe 2p XPS spectra and bonding in iron compounds, Surf. Interface Anal. 36 (12) (2004) 1564–1574, https://doi.org/10.1002/sia.1984.

[77] T. Yamashita, P. Hayes, Analysis of XPS spectra of Fe2+ and Fe3+ ions in oxide materials, Appl. Surf. Sci. 254 (8) (2008) 2441–2449, https://doi.org/10.1016/j.apsusc.2007.09.063.

[78] N. Eltouny, P.A. Ariya, Competing reactions of selected atmospheric gases on Fe3O4 nanoparticles surfaces, Phys. Chem. Chem. Phys. 16 (42) (2014) 23056–23066, https://doi.org/10.1039/C4CP02379J.

[79] K.F. Ngulube, A. Abdelhaleem, A.I. Osman, L. Peng, M. Nasr, Advancing sustainable water treatment strategies: harnessing magnetite-based photocatalysts and techno-economic analysis for enhanced wastewater management in the context of SDGs, Environ. Sci. Pollut. Res. (2024), https://doi.org/10.1007/s11356-024-32680-9.

[80] A. Kubiak, Comparative study of TiO2–Fe3O4 photocatalysts synthesized by conventional and microwave methods for metronidazole removal, Sci. Rep. 13 (1) (2023) 12075, https://doi.org/10.1038/s41598-023-39342-9.

[81] R. López, R. Gómez, Band-gap energy estimation from diffuse reflectance measurements on sol–Gel and commercial TiO2: a comparative study, J. Sol-Gel Sci. Technol. 61 (1) (2012) 1–7, https://doi.org/10.1007/s10971-011-2582-9.

[82] S. Delice, M. Isik, N.M. Gasanly, Temperature-dependent tuning of band gap of Fe3O4 nanoparticles for optoelectronic applications, Chem. Phys. Lett. 840 (2024) 141139, https://doi.org/10.1016/J.CPLETT.2024.141139.

[83] T. Saragi, B.L. Depi, S. Butarbutar, B. Permana, Risdiana. The impact of synthesis temperature on magnetite nanoparticles size synthesized by Co-precipitation method, J. Phys. Conf. Ser. 1013 (2018) 012190, https://doi.org/10.1088/1742-6596/1013/1/012190.

[84] E. György, A. Pérez del Pino, J. Roqueta, C. Sánchez, A.G. Oliva, Processing and immobilization of chondroitin-4-sulphate by UV laser radiation, Colloids Surf. B Biointerfaces 104 (2013) 169–173, https://doi.org/10.1016/j.colsurfb.2012.11.044.

[85] N.D. Abazović, M.I. Čomor, M.D. Dramićanin, D.J. Jovanović, S.P. Ahrenkiel, J. M. Nedeljković, Photoluminescence of anatase and rutile TiO 2 particles, J. Phys. Chem. B 110 (50) (2006) 25366–25370, https://doi.org/10.1021/jp064454f.

[86] L. Dai, F. Sun, P. Fu, H. Li, Enhanced photocatalytic hydrogen evolution and ammonia sensitivity of double-heterojunction g-C3N4/TiO2/CuO, RSC Adv. 12 (21) (2022) 13381–13392, https://doi.org/10.1039/D2RA01918C.

[87] L.M. Peter, A.B. Walker, T. Bein, A.G. Hufnagel, I. Kondofersky, Interpretation of photocurrent transients at semiconductor electrodes: effects of band-edge unpinning, J. Electroanal. Chem. 872 (2020) 114234, https://doi.org/10.1016/j.jelechem.2020.114234.

[88] T.F. Yeh, J. Cihlář, C.Y. Chang, C. Cheng, H. Teng, Roles of graphene oxide in photocatalytic water splitting, Mater. Today 16 (3) (2013) 78–84, https://doi.org/10.1016/J.MATTOD.2013.03.006.

[89] K. Villa, J.R. Galán-Mascarós, N. López, E. Palomares, Photocatalytic water splitting: advantages and challenges, Sustain. Energy Fuels 5 (18) (2021) 4560–4569, https://doi.org/10.1039/D1SE00808K.

[90] Q. Zhang, L. Yu, C. Xu, W. Zhang, M. Chen, Q. Xu, G. Diao, A novel method for facile preparation of recoverable Fe3O4@TiO2 core-shell nanospheres and their advanced photocatalytic application, Chem. Phys. Lett. 761 (2020) 138073, https://doi.org/10.1016/J.CPLETT.2020.138073.

[91] K.E. Dekrafft, C. Wang, W. Lin, Metal-organic framework templated synthesis of Fe2O3/TiO2 nanocomposite for hydrogen production, Adv. Mater. 24 (15) (2012) 2014–2018, https://doi.org/10.1002/ADMA.201200330.
[92] J.G. Villachica-Llamosas, J. Sowik, A. Ruiz-Aguirre, G. Colón, J. Peral, S. Malato, Photoreforming of glycerol to produce hydrogen from natural water in a compound parabolic collector solar photoreactor, J. Environ. Chem. Eng. 11 (6) (2023) 111216, https://doi.org/10.1016/J.JECE.2023.111216.
[93] S.A. Balsamo, R. Fiorenza, M.T.A. Iapichino, F.J. Lopez-Tenllado, F.J. Urbano, S. Sciré, H2 Production through glycerol photoreforming using one-pot prepared TiO2-RGO-Au photocatalysts, Mol. Catal. 547 (2023) 113346, https://doi.org/10.1016/J.MCAT.2023.113346.